Improving Leaf Area Index Estimation With Chlorophyll Insensitive Multispectral Red-Edge Vegetation Indices

Yuanheng Sun, Binyu Wang, and Zhaoxu Zhang

***Abstract*—As an essential vegetation biophysical trait that determines the plant's structure and photosynthetic capacity, characterizing of leaf area index (LAI) is important for vegetation growth and health monitoring. The empirical models based on vegetation indices (VIs) from remote sensing images are an effective method for deriving LAI. However, due to the coupled impacts of LAI and leaf chlorophyll content (LCC) on canopy reflectance and saturation effect, most VIs cannot achieve a good accuracy of LAI estimation. The remotely sensed red-edge reflectance can provide valuable information to delineate the LAI, therefore a series of leaf chlorophyll insensitive red-edge VIs by using the Sentinel-2 and GaoFen-6 (GF-6) multispectral images are developed in this work to improve the LAI estimation accuracy. The potentials of reflecting LAI variations and sensitivity to LCC changes for each Sentinel-2 and GF-6 red-edge band are comprehensively analyzed based on the PROSAIL model to select the optimal band in VIs design. The proposed VIs are then evaluated in multiple ways, including with PROSAIL simulated datasets, ground measured LAI with canopy spectra, and real satellite images. The evaluation results based on field LAI measurements indicate that the proposed red-edge VIs can effectively improve crop LAI estimation accuracy with the best regression coefficient ($R^2 = 0.81$ for Sentinel-2 and $R^2 = 0.65$ for GF-6) among all comparative VIs. Our work showcases incorporating red-edge bands with suitable formula is promising for improving VI-based LAI retrieval, and they offer a practicable solution to fast achieve decameter LAI maps by using the Sentinel-2 or GF-6 images.**

***Index Terms*—GaoFen-6 (GF-6), leaf area index (LAI), leaf chlorophyll, red-edge, Sentinel-2, vegetation index (VI).**

I. Introduction

VEGETATION plays an essential role in modulating the transfer and exchange of carbon, water, and energy between the terrestrial ecosystems and the atmosphere. Thus, it is of great importance to quantitively retrieve the vegetation biophysical and biochemical characteristics in many scientific realms [1], [2]. Among those vegetation characteristics, leaf area index (LAI), which is defined as the amount of leaf area in a canopy per unit of ground area [3], is closely related to a plant growing status and photosynthetic capacity [4], [5], therefore capturing the spatial and temporal variation of the LAI can provide critical information on the understanding of the global and regional vegetation health and carbon cycling [6], [7].

Traditional approaches for LAI measurement are based on destructively sampling foliage or nondestructively measuring with an optical instrument such as LAI-2000, which are labor-intensive and time-consuming [8]. A promising alternative is to use Earth observation techniques, and the remote sensing has been the only feasible way to acquire LAI over a vast area, especially at the global scale [9]. The methods of LAI deriving from optical images, which are the most widely used remotely sensed data source for LAI estimation, can be categorized into empirical and physical ones [10], [11]. The empirical methods directly establish the relationship between satellite-derived spectral characteristics, for instance, vegetation indices (VIs), and the LAI using statistical regression or advanced nonparametric models. This method is easy to implement but it requires different calibrations with field measurements for particular vegetation types or areas, and thus is not suitable for large scale continental and global LAI mapping [12]. The physical-based method uses a radiative transfer (RT) model that links the radiation intensity measured by satellite-borne sensors and the vegetation parameters, and the LAI is then retrieved with RT model inversion by taking sensor-measured reflectance and other auxiliary information as inputs. The physical methods are considered generalizing well across a wider area extent and yielding additional information about uncertainty of the retrievals, but they require more ancillary information for model parameterization, and the retrieval process is quite computational demanding [11].

The sensor measured canopy reflectance is affected by multiple factors, including biochemical parameters (e.g., chlorophyll content), biophysical parameters (e.g., LAI), and external conditions, such as atmosphere, soil background, and illumination/imaging geometry [13], [14]. Hence, the contributions from LAI and other parameters, especially the leaf chlorophyll content (LCC), to the canopy reflectance are often coupled. How to disentangle the individual contribution of the LAI and suppress the LCC signals in canopy reflectance is thus essential and indispensable for LAI estimation. Besides, spectral saturation issue often happens in the dense vegetated condition [15], [16],

Manuscript received 4 December 2022; revised 1 February 2023 and 6 March 2023; accepted 24 March 2023. Date of publication 28 March 2023; date of current version 12 April 2023. This work was supported by Fundamental Research Funds for the Central Universities of China under Grant 3132022136. *(Corresponding author: Yuanheng Sun.)*

Yuanheng Sun and Binyu Wang are with the Environmental Information Institute, Navigation College, Dalian Maritime University, Dalian 116026, China (e-mail: yhsun@dlmu.edu.cn; wby1120221062@dlmu.edu.cn).

Zhaoxu Zhang is with the School of Environmental Science and Engineering, Tiangong University, Tianjin 300387, China (e-mail: zhangzhaoxu_zzx@163.com).

Digital Object Identifier 10.1109/JSTARS.2023.3262643

and this further weaken the LAI estimating accuracy in large LAIs.

The red edge of a vegetation spectrum is defined as the sharp change in the reflectance curve between 680 and 750 nm [17], and it is observed highly sensitive to the variation of the LAI and LCC because the canopy reflectance in the red-edge region mainly results from the multiple scattering between leaf layers and chlorophyll absorption [18], [19]. Hence, it is a promising solution to improve the LAI retrieval accuracy by introducing the red-edge spectral information for both empirical and physical methods. Hyperspectral images containing red-edge information could delicately describe various characteristics of the vegetation biochemical and physiological traits [20]. As such, numerous methods such as hyperspectral vegetation index (VI) [21], [22], [23], spectral feature extraction, and machine learning algorithms [24], [25], [26] have been proposed to estimate the LAI by using hyperspectral remote sensing data. Even though hyperspectral image takes the advantage of containing more information for vegetation parameters retrieval, its disadvantages include limit spatial coverage and temporal frequency, high cost, low radiometric calibration accuracy, and more sophisticated and time-consuming process to do with the redundant band information [27], [28].

Multispectral images provide alternative options to the hyperspectral data for the LAI estimation with greater spatial and temporal coverage, which are very suitable for large scale vegetation monitoring in low cost. However, most traditional multispectral satellite sensors, such as Landsat TM/ETM+/OLI, do not customized with red-edge band settings for a long period. The multispectral red-edge sensor is originally equipped on commercial satellites, such as RapidEye [29], [30] and WorldView-2/WorldView-3 [31], [32], with meter-level spatial resolution. The first free-accessed decameter multispectral image with red-edge band setting for vegetation monitoring is the Sentinel-2 Multispectral Instrument (MSI) operated by Copernicus program of the European Space Agency (ESA). It provides three 20-m resolution narrow red-edge spectral bands in 5-day revisit period with Sentinel-2A and -2B constellation, which is thus of huge benefit to the LAI estimation [33], [34]. China's GaoFen-6 (GF-6) Wide Field View (WFV) image is another free-available decameter multispectral red-edge remotely sensed data supported by China Centre for Resources Satellite Data and Application. GF-6 WFV has two 16-m resolution red-edge multispectral bands located between red and near-infrared (NIR) domain, which is specifically designed for agricultural management and consequently shows great potentials in vegetation monitoring [35], [36].

VI is still the most extensive and effective remote sensing variable for LAI estimation due to its simplicity and computational efficiency, and it depicts the density or growth status of vegetation by using the contrast of spectral reflectance in different wavelengths [37]. The high reflective property in NIR and great absorptive property in red band of vegetation is the theoretical foundation for many VIs, which enhance the response of single band reflectance to the variation of LAI by using the ratio, difference, or normalized difference formation. Considering the unique advantages of red-edge characteristics, several VIs that incorporate red-edge bands have also been developed for LAI retrievals [34], [38], [39], [40], whereas most studies have only replaced visible or NIR bands with red-edge bands, which will inevitably increase the uncertainty of the resulting LAI retrievals due to the LCC affecting the reflectance of the red-edge bands. A few studies have also proposed several VIs to reduce the impacts of LCC on VI-based LAI inversions [10], [41]. However, these VIs still require empirical parameter to be adjusted. As such, the objective of this work is to comprehensively investigate the properties of Sentienl-2 and GF-6 multispectral red-edge band reflectance, and propose multispectral red-edge VIs, which are chlorophyll insensitive, and can resist saturation effect for LAI estimation.

The organization of this article is as follows. Section II describes the material utilized in this work, which includes PROSAIL simulation datasets, ground spectral and LAI measurements, and Sentinel-2, GF-6 and MODIS images. Detailed descriptions regarding the proposed multispectral red-edge VIs are described in Section III. The results of sensitivity analysis, evaluation, validation, and comparison based on multiple datasets are presented in Section IV. Section V discusses the applicability, causes of uncertainty, remaining issues to be improved, and perspective of the proposed VIs. Finally, Section VI concludes the article.

II. Material

A. PROSAIL Simulation

The PROSAIL model was used to simulate canopy reflectance with various combinations of leaf property, canopy structure, sun-sensor geometry, and background soil property, aiming to explore the Sentinel-2 and GF-6 red-edge spectral band characteristics and test the performance of the proposed multispectral red-edge VIs. This model couples the PROSPECT-D leaf optical properties model [42] and the scattering by arbitrarily inclined leaves (SAIL) canopy bidirectional reflectance model [43], which is widely used to simulate canopy spectra and to conduct sensitivity analysis [14]. To guarantee the size and representativeness of the simulated dataset, 20 000 spectra were simulated by randomly generating and combining the input parameters over a wide range, which are adequate to achieve stable analysis result. Table I lists the values or distributions of input parameters, and the truncated Gaussian or uniform distribution were adopted to generate the input variables for those whose value is varied within an interval. For the simulated dataset, the canopy spectral reflectance was further integrated into the band reflectance using the Sentinel-2/MSI and GF-6/WFV spectral filters (Fig. 1).

B. Ground Canopy Spectra Dataset and LAI Field Observations

In-situ datasets are used to evaluate the performance of the multispectral red-edge VIs at ground scale, and they were collected in Hengshui, Luohe, Chaoyang, and Kaifeng experimental sites from 2017 to 2020, respectively. The Hengshui experimental site locates at 37.5°N, 115.6°E, which has a warm

TABLE I
PARAMETER SETTINGS FOR PROSAIL MODEL USED FOR CANOPY REFLECTANCE MODELING

Type	Parameters	Values or distributions	Minimum value	Maximum value
Leaf	Leaf chlorophyll content (LCC, $\mu g/cm^2$)	Gauss(50, 20)	20	80
	Dry matter content (Cm, g/cm^2)	Gauss(0.009, 0.004)	0.005	0.013
	Leaf structure parameter (N)	Gauss(1.5, 0.5)	1	2
	Leaf carotenoid content (Ccar, $\mu g/cm^2$)	5	-	-
	Brown pigment content (Cbrown, $\mu g/cm^2$)	0	-	-
	Leaf anthocyanin content (Cant, $\mu g/cm^2$)	0	-	-
	Equivalent water thickness (Cw, cm)	0.01	-	-
canopy	Leaf area index (LAI, m^2/m^2)	Gauss(3, 1.5)	0.5	6.5
	Average leaf angle (ALA, degree)	Gauss(50, 10)	30	70
background	Soil moisture factor (ρsoil)	Uniform(0, 1)	0	1
Sun-target-sensor geometry	Solar zenith angle (SZA, degree)	Gauss(30, 10)	0	60
	View zenith angle (VZA, degree)	Gauss(10, 5)	0	20
	Relative azimuth angle (RAA, degree)	0	-	-

* The numbers in parenthesis for Gauss distribution represent mean value and standard deviation, and they represent lower bound and upper bound for Uniform distribution.

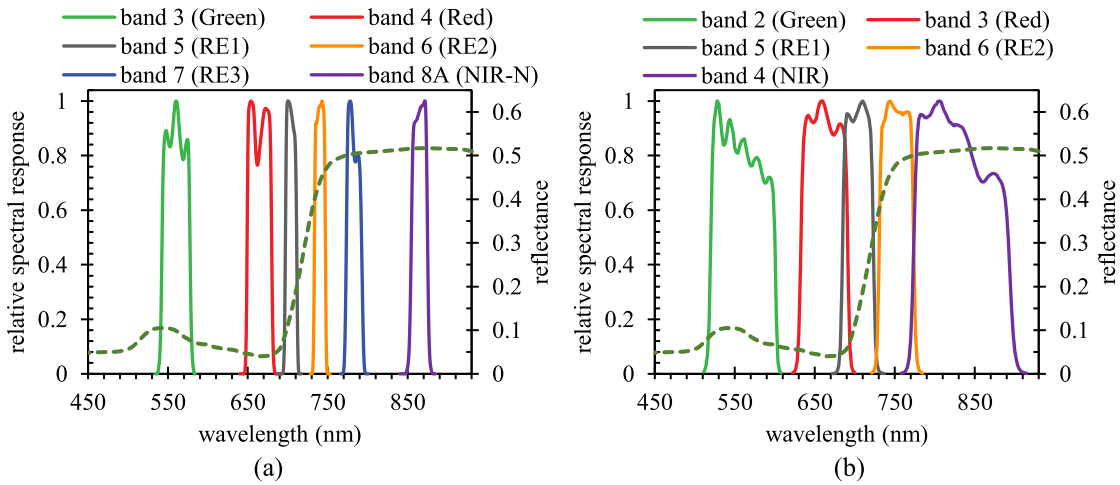

Fig. 1. Relative spectral responses of the red to NIR bands for (a) Sentinel-2 and (b) GF-6. The dark green dot line represents a typical conifer reflectance spectrum from the JHU spectrum library.

temperate monsoon (wet summer and dry winter) climate with a yearly average temperature of 12.7 °C and average precipitation of 510 mm. The Luohe experimental site has similar climate characteristics to that of Hengshui, with central geographical coordinates of 33.5°N and 115.6°E. The annual average temperature of the Luohe site is approximately 14.6 °C, and average precipitation is approximately 805 mm. Winter wheat (*Triticum aestivum L.*) and summer maize (*Zea mays L.*) are the main crops in both of those two regions and are under rotation irrigated management practices. The winter wheat is sowed in early October and harvested in early June (Hengshui) or late May (Luohe) of the next year, while the maize is cultivated from June to September. The location of the Chaoyang experimental site is approximately 41.9°N, 119.4°E. The continuously irrigated maize cultivated in Chaoyang is sowed in early May and harvested in October due to a relatively cold and more arid temperate monsoon climate, with annual temperature being 6.8 °C and precipitation of 480 mm. The Kaifeng experimental site centers at 34.9°N, 114.3°E and shares a similar climatic condition with Luohe. Because the date of field campaign carried out in Kaifeng was beyond the growing season of the cultivated wheat and maize, the type of vegetation that we took measurement there varied from birch, elm, aspen, and paddy rice. Detailed information of field observations is presented in Table II. Canopy spectra and LCC were measured only in Hengshui and Luohe, and the LAI was collected in all sites. All sample points were positioned in the homogeneous land cover with a spatial extent of at least 40 × 40 m.

The hyperspectral reflectance of the canopy was measured by an ASD FieldSpec Pro spectroradiometer (*Analytical Spectral*

TABLE II
DETAILED INFORMATION OF FIELD OBSERVATIONS

Experimental site with central Lat/Lon	Date	Vegetation type	Phenological stage	Observational targets	Number of samples
Hengshui (37.5°N, 115.6°E)	2017/3/30 – 2017/4/1	wheat	jointing	LAI, LCC, canopy spectra	45
	2017/5/5 – 2017/5/7	wheat	heading	LAI, LCC, canopy spectra	42
	2017/7/3 – 2017/7/5	maize	seeding	LAI, LCC	18
	2017/7/29 – 2017/8/1	maize	grain-filling	LAI, LCC	21
Luohe (33.5°N, 115.6°E)	2018/3/11 – 2018/3/14	wheat	jointing	LAI, LCC, canopy spectra	32
	2018/4/11 – 2018/4/14	wheat	heading	LAI, LCC, canopy spectra	28
Chaoyang (41.9°N, 119.4°E)	2018/6/16 – 2018/6/18	maize	seeding	LAI	24
Kaifeng (34.9°N, 114.3°E)	2020/10/14 – 2020/10/19	-	-	LAI	30

Devices, Inc., Boulder, CO, USA) covering the spectral range from 350 to 2500 nm with a resampled interval of 1 nm. Five positions in a sample point were randomly selected for measurement to reduce the impact of environmental conditions, and the average value was used as the representative spectral reflectance of the sample point, which was further integrated into the band reflectance using the Sentinel-2/MSI and GF-6/WFV spectral filters.

The LAI was measured using a LAI-2000 Plant Canopy Analyzer (*Li-Cor Inc., Lincoln, NE, USA*). Since all the green parts of crops are detected during measurements, the measured total LAI can be understood as "effective green PAI" according to its definition.

The SPAD-502 chlorophyll meter (*Konica Minolta, Inc.*) was used to measure the LCC. Four replicate measurements were conducted in the upper, middle, and lower levels of the wheat canopy within a sample point, and the twelve readings were averaged to calculate the SPAD value of the canopy. The SPAD measurements were then converted to LCCs through (1) [44], [45].

$$\mathrm{LCC} = 6.34299 \times \exp\left(\mathrm{SPAD} \times 0.043\right) - 6.10629. \quad (1)$$

C. Remote Sensing Data

The dates of the Sentinel-2 images used in this work are concurrent with those of the ground canopy spectra and LAI measurements in Hengshui, Luohe, and Chaoyang sites, and spatially covers them. The images were downloaded from the ESA Sentinels Scientific Data Hub[1] as Level-1C orthorectified top of atmosphere reflectance and then atmospherically corrected to obtain the surface reflectance using the Sen2Cor atmosphere correction toolbox (version 2.5.5) built in the Sentinel Application Platform (SNAP) software (version 6.0.0). The spatial resolutions of all bands were set to 20 m to guarantee the combined use of green, red, and NIR bands with three red-edge bands (RE1, RE2, and RE3) and narrow NIR band (NIR-N) in the atmospherically corrected images [33]. The LAI was further calculated based on their band surface reflectance with proposed red-edge VI, and the empirical VI-LAI relationship was derived with specific ground LAI measurements collected at Hengshui and Luohe.

[1][Online]. Available: http://scihub.copernicus.eu/

The dates of GF-6 images are matching that of the field works in Kaifeng, and they were downloaded from the China Centre for Resources Satellite Data and Application platform.[2] The GF-6 images were first geometric corrected with the RPC Orthorectification module embedded in the ENVI software (version 5.3), and then processed in radiometric calibration and atmospheric correction with ENVI FLAASH module. The spatial resolution of output GF-6 atmospherically corrected and orthorectified images were set to 16 m for all the visible, red-edge, and NIR bands.

Besides, the Terra and Aqua MODIS Collection 6 (C6) 4-day composite LAI products (MCD15A3H) for the period of 2018 and 2019 over Hengshui and Luohe are utilized for comparison with time-series LAI derived from Sentinel-2 images [46], [47]. The data are downloaded from NASA's Earth Data platform,[3] and only MODIS LAI pixels generated by the main algorithm are retained with the assist of its ancillary quality-control labels.

III. METHODS

A. Correlation and Sensitivity Analysis for Bands Selection

To select bands that are sensitive to the variation of canopy LAI but not sensitive to the variation of LCC, we calculated the Pearson correlation coefficient (R) to analyze the correlation between reflectance at each band of Sentinel-2 or GF-6 and the LAI or LCC (2) based on PROSAIL simulations. Pearson correlation coefficient characterizes the linear correlation (dependence) between two variables x and y, whose range varies from -1 to 1, where 1 means totally positive linear correlation, 0 means no linear correlation, and -1 means totally negative linear correlation.

$$R = \frac{\sum_{i=1}^{n}\left(X_i - \bar{X}\right)\left(Y_i - \bar{Y}\right)}{\sqrt{\sum_{i=1}^{n}\left(X_i - \bar{X}\right)^2 \sum_{i=1}^{n}\left(Y_i - \bar{Y}\right)^2}}. \quad (2)$$

Here, we calculated the Pearson correlation coefficients for all the visible to NIR bands of Sentinel-2 and GF-6 with the LAI and LCC, and their results are shown in Fig. 2. The LAI shows the strongest positive correlation with RE3, NIR, NIR-N of Sentinel-2, while the strongest negative correlation is found at red band. Compared with RE3 and NIR bands, the correlation

[2][Online]. Available: https://data.cresda.cn/#/home
[3][Online]. Available: https://www.earthdata.nasa.gov/

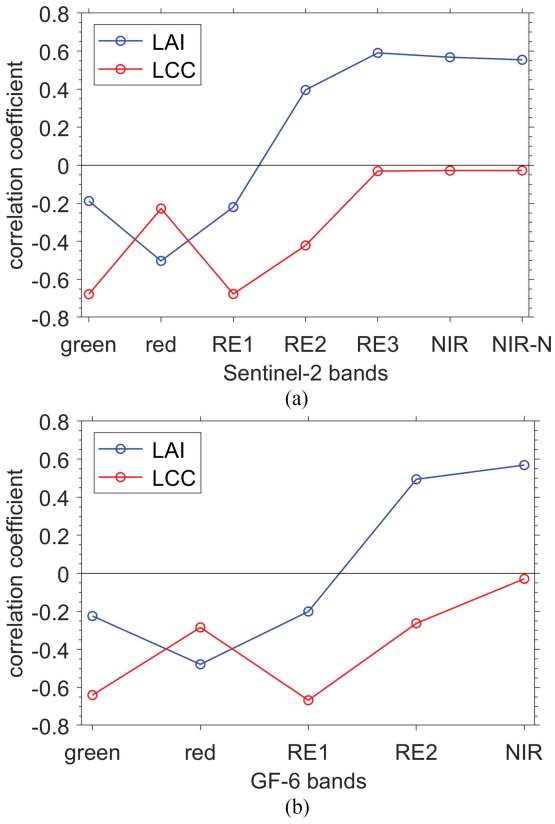

Fig. 2. Pearson correlation coefficients of band reflectance and LAI or LCC for (a) Sentinel-2 and (b) GF-6 based on the PROSAIL simulated dataset.

between RE2 and LAI decreases slightly, and the green and RE1 bands present the lowest correlation with LAI. The strongest negative correlation between LCC and band reflectance emerges in the green and RE1 bands of Sentinel-2, while the red and RE1 represent weak negative correlation with the LCC.

For GF-6 multispectral bands reflectance, significant positive correlations with LAI are presented at RE2 and NIR and greatest negative correlation is shown at red, while the green and RE1 bands have low correlation relationship with the LAI. Obvious positive correlations with LCC are present at green and RE1, and the correlation coefficient gradually decreases for red and RE2 and approaches 0 for NIR.

The influence of a single parameter is rarely completely independent, and coupling interactions usually exist between various parameters (e.g., LAI and LCC). Thus, the extended Fourier amplitude sensitivity test (EFAST) approach which can describe the coupling interactions was adopted in this study [48], [49]. The EFAST approach is a feature importance ranking method that can evaluate the contribution of each variable to the Sentinel-2 and GF-6 band reflectance simulated with the PROSAIL model with high computational efficiency. In this practice, the calculation by EFAST is limited to sensitivities referring to the main effect (additive influence of individual input factor) and total effect (an overall measurement of the contribution of a factor coupling with others). This work conducted the EFAST global sensitivity analysis with the Sensitivity Package (version 1.15.2) on the R platform (version 3.5.1).

Figs. 3 and 4 present the main effect and total effect of each influencing factor on the Sentinel-2 and GF-6 green to NIR band reflectance. The green band of Sentinel-2 and GF-6 show similar characteristics, and the impact of LCC maintains dominance among all influencing factors [Figs. 3(a) and 4(a)]. The LAI contributes most to the red band reflectance of Sentinel-2 and GF-6 [Figs. 3(b) and 4(b)]. However, great interaction effect can be observed from LAI with other factors, for instance, soil moisture, and the main effect of LCC is nonignorable.

The RE1 band of Sentinel-2 and GF-6 also have similar characteristics, and their top 5 influencing factors from the perspective of main effect are LCC, leaf structure, LAI, soil property, and ALA, which is almost the same as the sensitivity of green band. Because the central wavelength of Sentinel-2 RE1 band is closer to red spectral domain and it has a narrower bandwidth compared with that of GF-6 RE1, more contribution from the LCC is observed in the Sentinel-2 RE1 band [Figs. 3(c) and 4(c)]. Considering the total effect which is defined as the sum of main effect and interaction, the influence of LAI and soil property mainly comes from their interactions coupled with other factors. Hence, it may introduce more uncertainty by using the RE1 band of Sentinel-2 and GF-6 in LAI estimation even though it does have a certain influence from the LAI.

Top 5 influencing factors for Sentinel-2 RE2 band are LAI, ALA, LCC, leaf structure, and soil property from the perspective of main effect [Fig. 3(d)]. Despite the LAI contributes most to the Sentinel-2 RE2 band, it still has large interaction effect with other factors. Top 5 influencing factors for GF-6 RE2 band are LAI, ALA, soil property, leaf structure, and leaf dry matter [Fig. 4(d)]. The contribution of LAI dramatically increases and that of LCC dramatically decreases compared with GF-6 RE1 band. For Sentinel-2 RE3, NIR-N, and GF-6 NIR, the contribution of LAI is dominant compared with other factors and the LCC hardly influences their reflectance [Figs. 3(e), (f), and 4(e)]. Thus, they are optimal red-edge bands for LAI estimation.

Based on the above-mentioned analysis, it can be concluded that the RE3 band of Sentinel-2 and NIR band of GF-6 contain the most information of LAI in a positive correlated direction, and the red band shows a negative correlation relationship with the LAI. The green and RE1 bands of Sentinel-2 and GF-6 are severely affected by the chlorophyll content, whereas their red and RE2 bands are moderate sensitive to the LCC influence with a negative correlation.

B. *Multispectral Red-Edge VIs for LAI Estimation*

In this work, simple ratio (SR) [50], normalized difference vegetation index (NDVI) [51], and modified simple ratio (MSR) [52] are selected as the prototype for further red-edge VIs design, whose equations are listed in the following:

$$\mathrm{SR} = \frac{\rho_{\mathrm{NIR}}}{\rho_{\mathrm{Red}}} \tag{3}$$

$$\mathrm{NDVI} = \frac{\rho_{\mathrm{NIR}} - \rho_{\mathrm{Red}}}{\rho_{\mathrm{NIR}} + \rho_{\mathrm{Red}}} \tag{4}$$

$$\mathrm{MSR} = \frac{\rho_{\mathrm{NIR}}/\rho_{\mathrm{Red}} - 1}{\sqrt{\rho_{\mathrm{NIR}}/\rho_{\mathrm{Red}} + 1}} \tag{5}$$

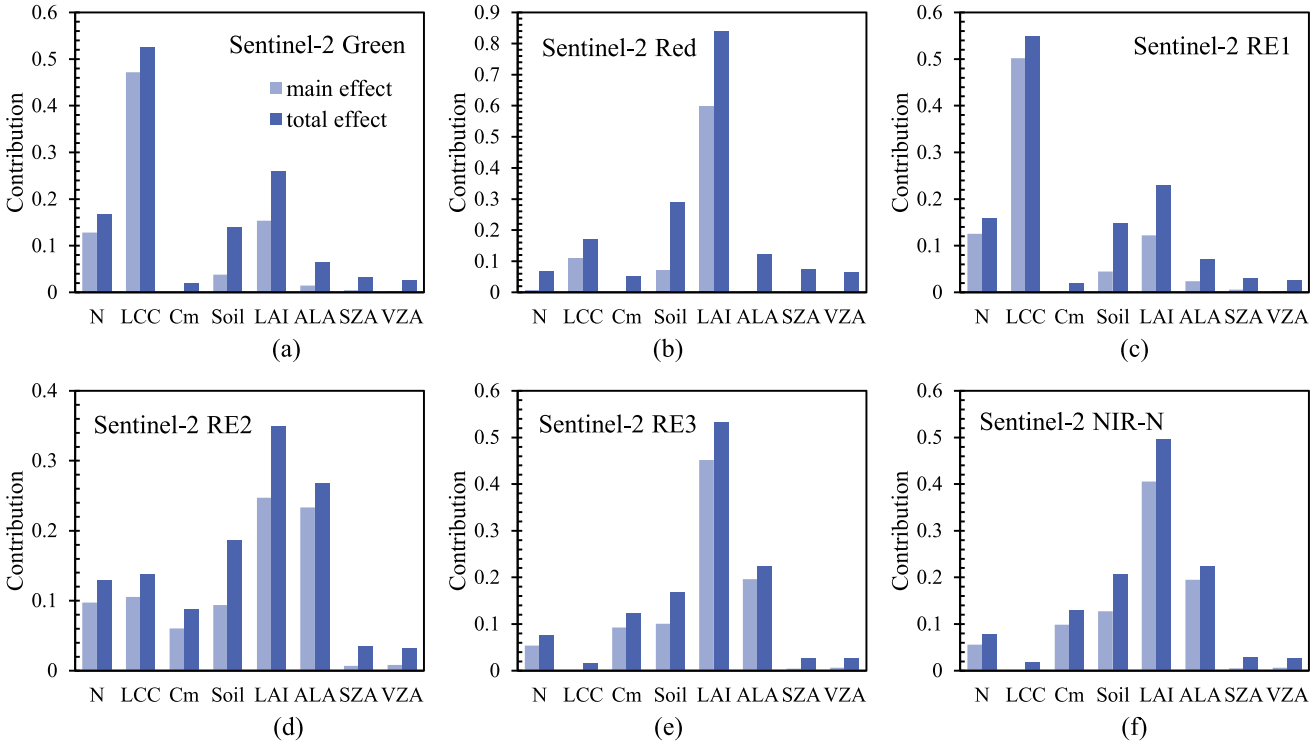

Fig. 3. Main and total effect of each influencing factor to the spectral reflectance of Sentinel-2 green to NIR bands with the EFAST sensitivity analysis and the PROSAIL model. (a) Green. (b) Red. (c) RE1. (d) RE2. (e) RE3. (f) NIR-N.

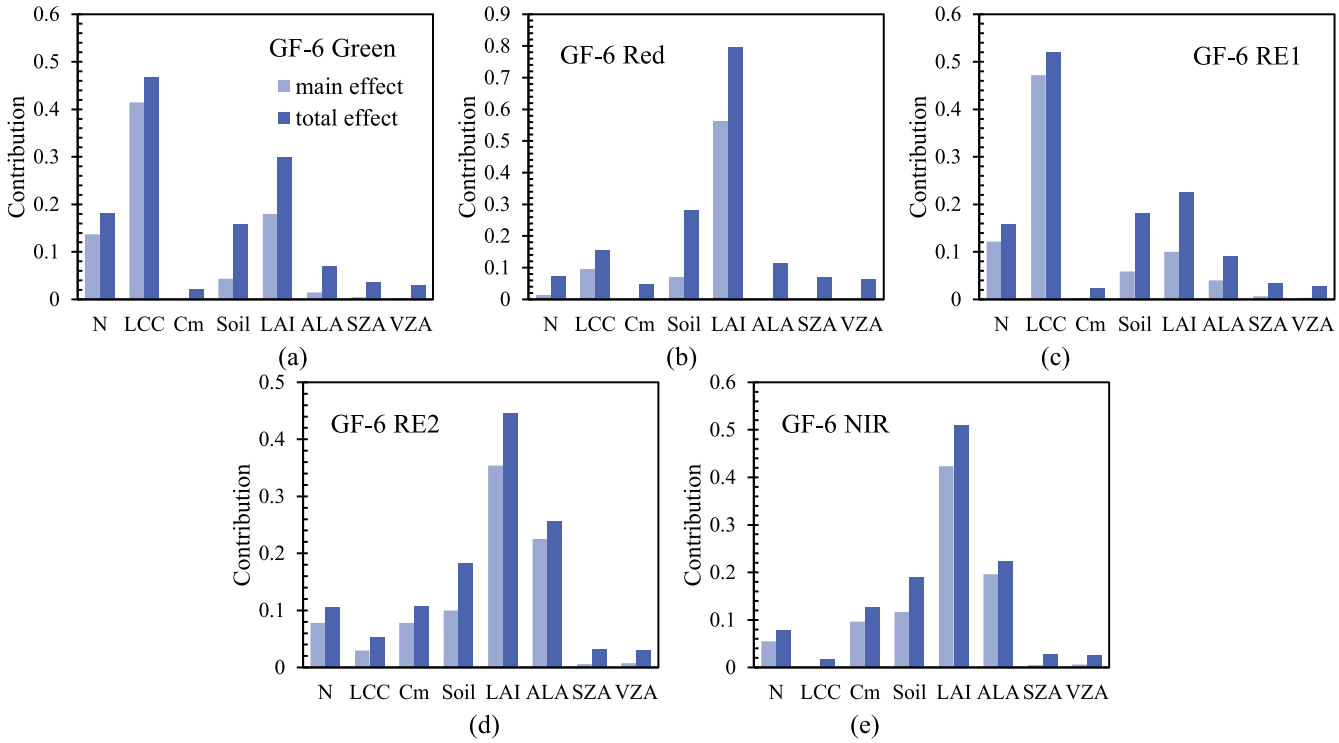

Fig. 4. Main and total effect of each influencing factor to the spectral reflectance of GF-6 green to NIR bands with the EFAST sensitivity analysis and the PROSAIL model. (a) Green. (b) Red. (c) RE1. (d) RE2. (e) NIR.

TABLE III
PROPOSED MULTISPECTRAL RED-EDGE VIS FOR SENTINEL-2 AND GF-6

	Sentinel-2	GF-6
SR formation (SR_{re})	$\frac{\rho_{RE2} \times \rho_{RE3}}{\rho_{Red}}$	$\frac{\rho_{RE2} \times \rho_{NIR}}{\rho_{Red}}$
NDVI formation ($NDVI_{re}$)	$\frac{\rho_{RE2} - \rho_{Red}}{\rho_{RE2} + \rho_{Red}} \times \rho_{RE3}$	$\frac{\rho_{RE2} - \rho_{Red}}{\rho_{RE2} + \rho_{Red}} \times \rho_{NIR}$
MSR formation (MSR_{re})	$\frac{\rho_{RE2}/\rho_{Red} - 1}{\sqrt{\rho_{RE2}/\rho_{Red} + 1}} \times \rho_{RE3}$	$\frac{\rho_{RE2}/\rho_{Red} - 1}{\sqrt{\rho_{RE2}/\rho_{Red} + 1}} \times \rho_{NIR}$

where ρ_{Red} and ρ_{NIR} represent the canopy reflectance of multispectral red and NIR band, respectively.

As the correlation and sensitivity analysis show, the red band reflectance of Sentinel-2 and GF-6 is influenced by both LAI and LCC, hence most VI is the comprehensive measuring of vegetation "greenness". If these VIs are utilized for LAI estimation, the impact of the LCC variation is inevitable. Since the negative correlation coefficients of red and RE2 bands of Sentinel-2 with LCC are roughly equal, and the RE2 band of Sentinel-2 shows high positive correlation with LAI simultaneously, the RE2 band of Sentinel-2 is introduced in the design of red-edge VIs to offset a portion of impact from LCC introduced by red band reflectance. Similarly, RE2 band is also used in GF-6 multispectral red-edge VIs. To enhance the sensitivity of newly proposed red-edge VIs in dense vegetated condition and to relieve the saturation effect, we multiply the original VI formation by the reflectance of Sentinel-2 RE3 band or GF-6 NIR band, which are principally and highly positively correlated with LAI, following the idea of NIR_v [53], [54]. The proposed multispectral red-edge VIs for Sentinel-2 and GF-6 are listed in Table III.

C. Evaluation and Validation Metrics

If the variation of LAI or LCC leads to great change to the VI value, we regard this VI is sensitive to the LAI or LCC, and *vice versa*. Besides, if the amplitude of VI value is large when the LAI is fixed while other factors vary in a specific range, large uncertainty may occur in LAI estimation by using this VI. We use these properties to qualitatively evaluate the sensitivity of proposed the red-edge VIs toward the variation of LAI and LCC. Moreover, the performance of the proposed red-edge VIs in LAI retrieval was quantitatively validated using the coefficient of correlation (R) and coefficient of determination (R^2) when compared with field measured LCC.

IV. RESULTS

A. Sensitivity of Proposed Multispectral Red-Edge VIs With PROSAIL Simulation

The qualitative sensitivity analysis of the proposed VIs was implemented by using the PROSAIL simulated dataset. To explore the influence of LCC to the VIs, we set the LCC value from 20 $\mu g/cm^2$ to 80 $\mu g/cm^2$ with a step of 5 $\mu g/cm^2$. The value or distribution of other PROSAIL input parameters were referred in Table I. For the LAI sensitivity analysis, its value was set from 0.5 to 6.5 with a step of 0.5 with other parameters varying as Table I.

Fig. 5 illustrates the response of the original SR, NDVI, MSR, and proposed red-edge VIs to the variation of LCC for Sentinel-2 and GF-6. The shaded area represents the ± 1 standard deviation error. In general, the value of original VIs increases as the LCC increases. Under the low LCC circumstance (LCC < 40 $\mu g/cm^2$), the value of original VIs greatly increases while red-edge VIs in SR and MSR formation only slightly increases with the LCC increasing. What is more, the value of Sentinel2 $NDVI_{re}$ almost does not change when the LCC varies, and the GF6 $NDVI_{re}$ slightly decreases as LCC increasing. Since the value of LCC of vegetation in the growing seasons centers at the interval of 40–65 $\mu g/cm^2$ according to our fieldwork and all proposed Sentinel-2 and GF-6 red-edge VIs almost stay unchanged, it is believed that the original VIs and proposed multispectral red-edge VIs are insensitive to the variation of LCC in most circumstances. However, the uncertainty of the multispectral red-edge VIs caused by other factors is still large in the LCC interval of 40–65 $\mu g/cm^2$, which should be paid attention to in the application.

The main purpose of those proposed Sentinel-2 and GF-6 red-edge VIs is to effectively reflect the variation of LAI. The value of those VIs significantly increases as LAI increasing, as Fig. 6 shows, but difference exists in the uncertainty toward other factors and saturation effect under dense vegetated condition. The sensitivity of proposed red-edge VIs is significantly higher than that of original VIs in dense vegetated condition. With LAI increases from 4.0 to 6.0, the value of red-edge VIs in SR, NDVI, and MSR formation increases 20.66%, 9.15%, and 15.52%, while that are 16.31%, 1.39%, and 9.07% for their original formation. Among the proposed red-edge VIs, the red-edge VI in NDVI formation has the lowest uncertainty, but it also has the minimum saturation point – the increment of VI value is limited as LAI increases when LAI is greater than 3.5. Compared with red-edge VI in NDVI formation, SR formation VI shows greater saturation point. However, the uncertainty of it also magnifies in large LAI condition. The red-edge VI in MSR formation balances the advantage of VI in SR and NDVI formation, with a relative low uncertainty and saturation effect, thus is regarded as an ideal chlorophyll insensitive option to estimate LAI.

B. Evaluation With Ground Canopy Spectra Dataset

We further evaluate the proposed Sentinel-2 and GF-6 red-edge VIs with ground measured canopy spectra and corresponding LAI and LCC dataset collected in Hengshui and Luohe (Table II), and compare them with some classic VIs or VIs without using red-edge information. The classic VIs include SR, NDVI, and MSR. The RE2 and RE3 in proposed Sentinel-2 red-edge VIs are replaced by NIR-N band, while the RE2 in GF-6 red-edge VIs is replaced by its NIR band in the VIs without using red-edge information. The coefficients of correlation (R) between a specific VI derived from ground measured spectra and the LAI or LCC are calculated to represent their correlation degree, which are shown in Table IV.

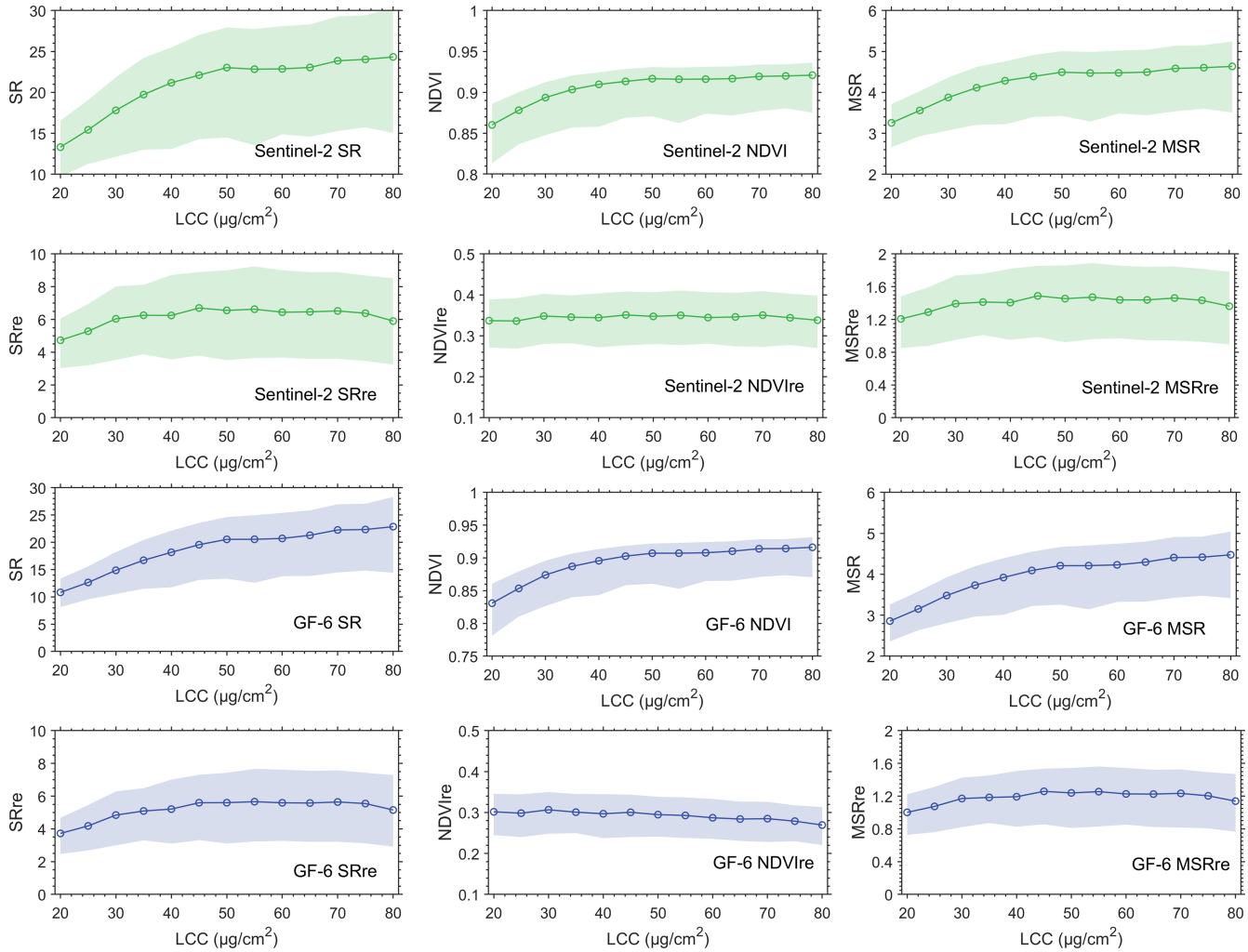

Fig. 5. Sensitivity of the original SR, NDVI, MSR, and proposed red-edge VIs to LCC for Sentinel-2 (first two rows) and GF-6 (last two rows) derived based on the PROSAIL model [14]. The shaded area represents the ±1 standard deviation error.

TABLE IV
CORRELATION COEFFICIENTS (R) OF SENTINEL-2 OR GF-6 VIS AND LAI OR LCC BASED ON GROUND SPECTRA OBSERVATIONS

		With red-edge bands			Without red-edge bands			Classic vegetation indices		
		SR	NDVI	MSR	SR	NDVI	MSR	SR	NDVI	MSR
Sentinel-2	LAI	0.58	0.71	0.65	0.57	0.64	0.64	0.39	0.44	0.43
	LCC	-0.19	-0.28	-0.22	-0.21	-0.28	-0.23	0.02	0.15	0.05
GF-6	LAI	0.59	0.66	0.62	0.58	0.64	0.62	0.40	0.44	0.43
	LCC	-0.20	-0.29	-0.23	-0.21	-0.28	-0.24	0.03	0.15	0.06

The correlation between VI and LAI significantly increases after the red-edge bands are introduced for Sentinel-2 NDVI formation, and that of VIs in Sentinel-2 SR and MSR formation varies little before and after red-edge spectral information is utilized. All the three red-edge VI formations manifest similar correlation coefficient with or without using red-edge spectral information. The classic SR, NDVI, and MSR, both for Sentinel-2 and GF-6, demonstrate the lowest correlation relationship with the LAI. For the LCC, there is no remarkable difference in the correlation between it and various VIs with or without using red-edge information, which may be attributed to the large uncertainty of field measured LCC.

C. Validation With Sentinel-2 and GF-6 Images

The proposed Sentinel-2 and GF-6 red-edge VIs and classic VIs for comparison are then validated by using real Sentinel-2 and GF-6 images and their synchronized ground LAI datasets. The LAI datasets collected in Hengshui, Luohe, and Chaoyang are used for Sentinel-2 validation, and the LAI collected in Kaifeng are used for GF-6 validation. The symbol of SR_{re}, $NDVI_{re}$, and MSR_{re} in Figs. 7 and 8 represent the proposed multispectral red-edge VIs in SR, NDVI, and MSR formation, while the SR_{nir}, $NDVI_{nir}$, and MSR_{nir} represent the VI formation of SR, NDVI, and MSR without using red-edge bands. Here, we

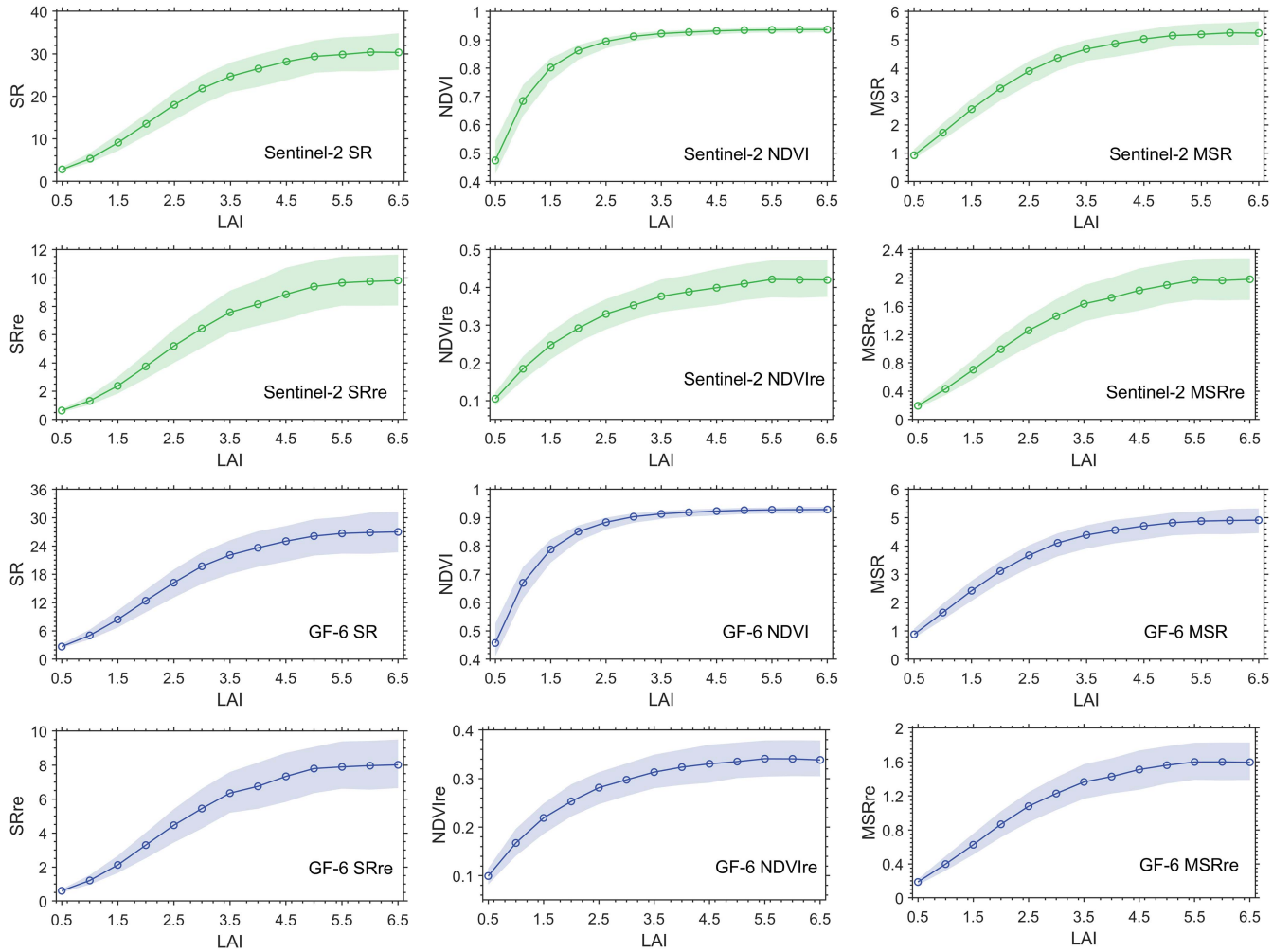

Fig. 6. Sensitivity of the original SR, NDVI, MSR, and proposed red-edge VIs to LAI for Sentinel-2 (first column) and GF-6 (second column) derived based on the PROSAIL model [14]. The shaded area represents the ±1 standard deviation error.

adopt the coefficient of determination (R^2) to investigate in what degree the LAI could be explained by a VI when using it in LAI estimation. Sentinel-2 results demonstrate that the determination coefficient remarkably improves after the red-edge bands are used, and it also relieves the saturation effect in large LAI condition for NDVI (Fig. 7). The determination coefficient of proposed GF-6 red-edge VIs also improves compared with VIs without red-edge bands. Due to limit validating samples and ground measured uncertainties in LAI, the resistance to the saturation effect of classic VIs is not profound when red-edge bands are introduced.

Based on the evaluations with ground canopy spectra and real Sentinel-2 and GF-6 images, the proposed multispectral red-edge VI demonstrates effective enhancement to the correlation relationship with LAI compared with those classic VIs.

D. LAI Mapping and Time-Series Analysis With Sentinel-2 Images

In this section, the regional LAI mapping covering Hengshui and Luohe experimental sites are generated by using the proposed Sentinel-2 red-edge VI in NDVI formation ($NDVI_{re}$). Meanwhile, time-series of Sentinel-2 derived LAI extracted from one of Hengshui or Luohe samples are then compared with MODIS LAI product to preliminary explore whether they can reveal the phenology of LAI of wheat and maize, and to what extent their consistency is with the most widely used MODIS LAI. The geographic coordinates of the Hengshui sample are (115.47°E, 37.87°N), and that of Luohe sample are (114.17°E, 33.65°N). Both sites are located at homogeneous cropland to reduce the scale effect caused by different spatial resolution between Sentinel-2 and MODIS data.

The LAI images of nonvegetated areas extracted on March 23 and May 2 of 2017, corresponding to moderate and dense vegetated conditions, in Hengshui are presented in Fig. 9. The mean LAI value over the region is 1.4 in March and 3.8 in May. Fig. 10 illustrates the LAI images in Luohe on February 27 and April 13 of 2018, with mean LAI of 0.8 in February and 3.5 in April.

Figs. 9(c) and 10(c) show the temporal LAI trajectories over the two sites for the entire year of 2017 or 2018. For a better

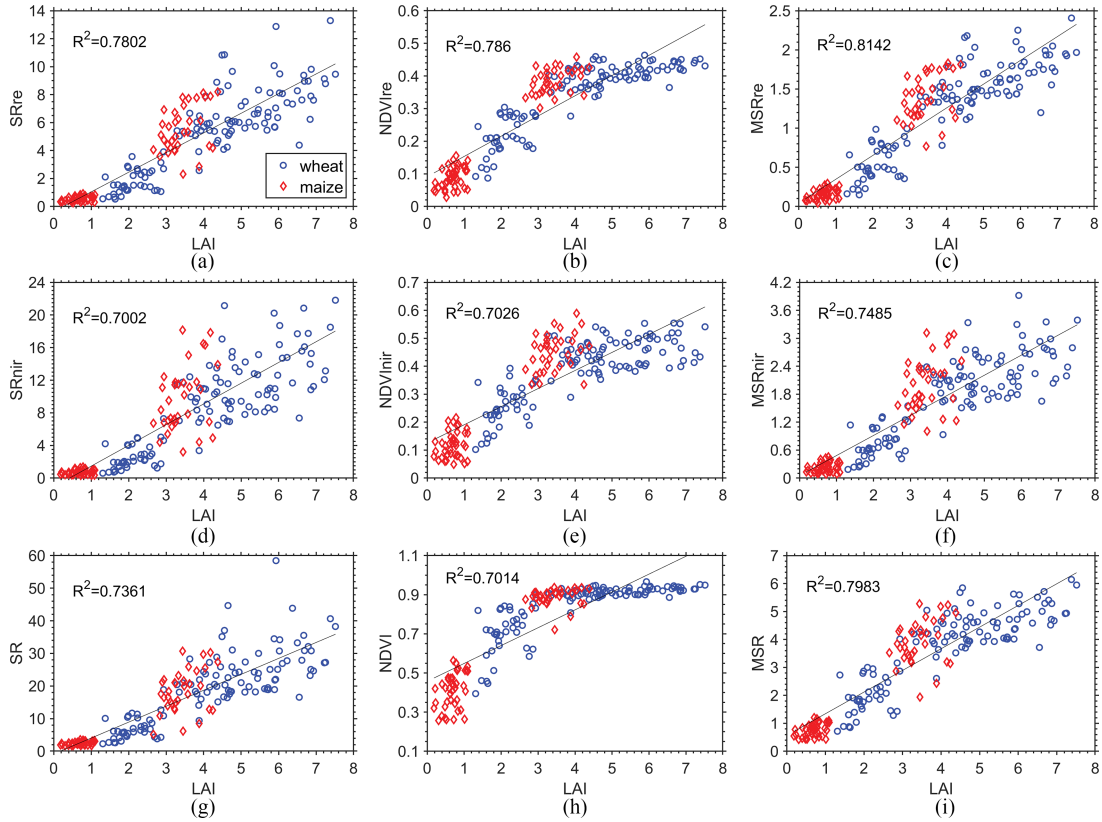

Fig. 7. Scattering plots of ground measured LAI and Sentinel-2 derived proposed red-edge VIs (upper row), proposed VIs without using red-edge bands (middle row), and classic VIs (bottom row).

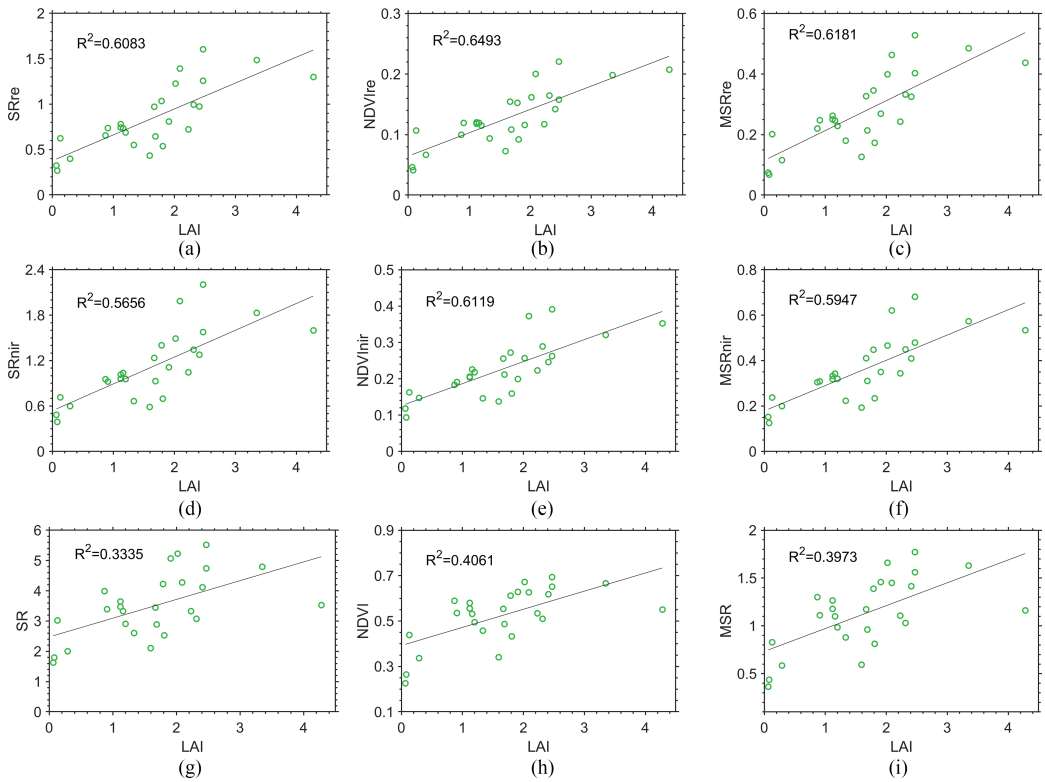

Fig. 8. Scattering plots of ground measured LAI and GF-6 derived proposed red-edge VIs (upper row), proposed VIs without using red-edge bands (middle row), and classic VIs (bottom row).

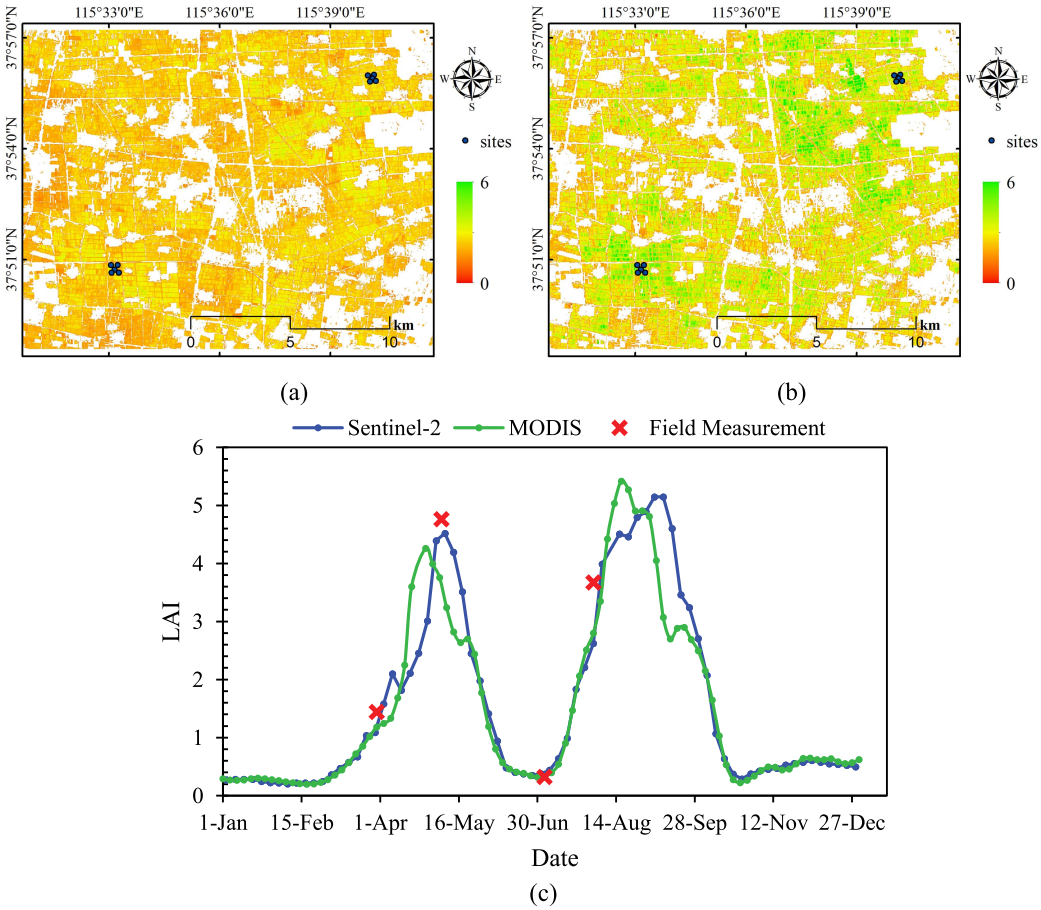

Fig. 9. LAI mapping over Hengshui experimental sites on (a) March 23 of 2017 and (b) May 2 of 2017. (c) LAI time series derived from Sentinel-2 and MODIS in 2017 of a specific site.

comparison, Sentinel-2 results are aggregated to 500 m to match the MODIS resolution, and both LAI trajectories are processed with a Savitzky–Golay smoothing filter. The bimodal pattern of LAI seasonality over the two sites is caused by rotation agricultural management of wheat and maize during a year, and the peak of wheat growing appears in April to May and maize in August to September, which are influenced by its latitude [55]. The Sentinel-2 and MODIS LAI are in good agreement in the entire year, and they both agree well with field measurements. A few mismatches between Sentinel-2 and MODIS LAI only show in the extreme high vegetated condition, which may attribute to different composite or imaging period, and smoothing filter influence.

V. Discussion

Quantitative acquisition of widespread vegetation LAI with remote sensing techniques is essential for numerous environmental and agricultural studies and applications [9], [56]. LAI retrieval using red-edge information has attracted much attention, and the community-consensual view is that red-edge bands have a positive contribution to LAI inversion [10], [21], [57]. Compared with hyperspectral red-edge data, studies on multispectral red-edge band in LAI estimation is still limit and some have indicated that they are not significantly beneficial for LAI retrieval [58], [59]. As a result, it is necessary to further and fully explore the spectral characteristics of existing multispectral red-edge bands and develop new VIs for LAI estimation with them [58].

The red-edge reflectance is usually influenced by various vegetation characteristics; thus, the integration of red-edge information in LAI estimation may increase the canopy information contents effectively representing the LAI or may be coupled with other vegetation characteristics. For instance, previous studies have suggested that Sentinel-2 red-edge bands contribute more to the LCC estimation [60], [61], so the high sensitivity of LCC would in turn reduce the LAI estimation accuracy if all three Sentinel-2 red-edge bands are introduced. The proposed red-edge VIs with Sentinel-2 and GF-6 multispectral red-edge bands in this article aim to reduce the LCC and saturation effect for LAI estimation. Since the interactions between LAI and LCC to the canopy reflectance remain a challenge when identifying canopy reflectance changes caused by LAI variations, the PROSAIL simulations enable us to comprehensively understand the effects of variations in LAI and other parameters on the band reflectance, thus providing an effective way to develop the VIs

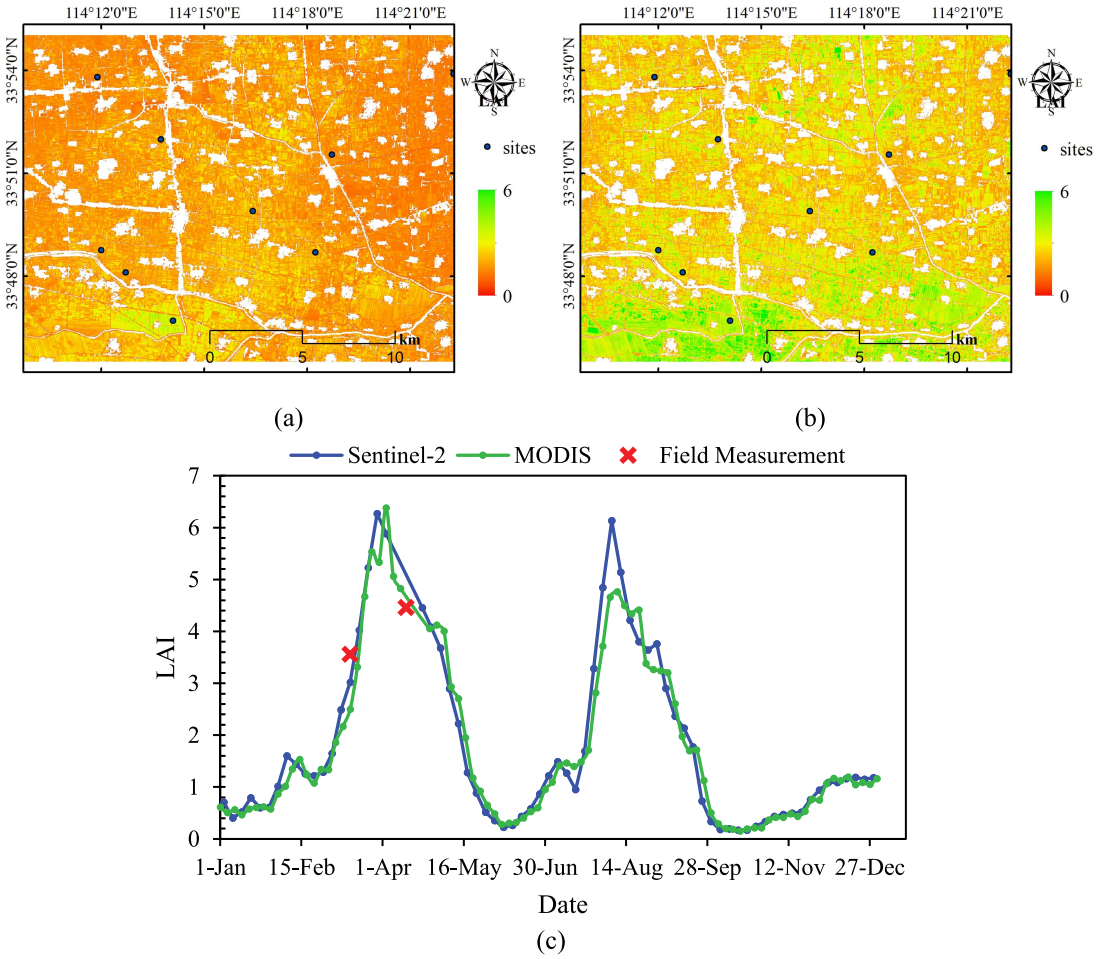

Fig. 10. LAI mapping over Luohe experimental sites on (a) February 27 of 2018 and (b) April 13 of 2018. (c) LAI time series derived from Sentinel-2 and MODIS in 2018 of a specific site.

using the specific advantages of Sentinel-2 and GF-6 red-edge bands.

The proposed Sentinel-2 and GF-6 red-edge VIs were then evaluated and compared against some classic VIs in several scales: simulated datasets, ground canopy spectra, and real satellite images. The improvement of correlation coefficient is not quite profound after the red-edge bands are introduced in ground canopy spectra scale, and possible explanations may be the inevitable uncertainty of ground measured canopy spectral and LCC caused by measuring time, weather condition, and the proficiency level of operators [8]. The ground collected SPAD signal by a SPAD-502 instrument was converted to the true LCC by using the empirical equations [45], which depends on vegetation type, and this kind of conversion also introduces the LCC uncertainty. The VIs in SR formation magnify and the VIs in NDVI formation compress the uncertainty, therefore, the best performance comes from VI in MSR formation, and SR formation performs the worst at ground scale validation. The performance of red-edge VIs derived from real Sentinel-2 and GF-6 images in LAI estimation is better compared with that derived from ground canopy spectra (Figs. 7, 8, and Table IV). This is because our ground LAI was evenly collected in homogenous vegetated area and is representative to an entire satellite image pixel, thus the relationship between the pixel VI value and the *in-situ* LAI is more stable comparing the ground spectra results.

However, the evaluations cannot represent all potential vegetated scenarios due to insufficient ground LAI datasets for validation. Thus, the proposed VIs are specifically suitable for crop application at present, and further validation in other biome type is needed. Adding more field measurements, especially from various biome types, time periods, and regions, may allow more comprehensive evaluation results to be obtained. However, due to the intricate coupling of canopy parameters and the limited spectral bands of multispectral sensors, it is impractical to develop a VI that is not sensitive to all biophysical and biochemical parameters. Note that the ALA also greatly impacts the values of RE2 (Figs. 3 and 4), and our sensitivity analysis showcases that the proposed red-edge VIs are in turn sensitive to the variation of ALA. As a result, much attention should be paid when using them in LAI estimation, especially at regions or periods with varied ALA. Nevertheless, the main vegetation types may be similar within a certain region and period, which could mitigate the negative effects caused by the sensitivity toward other parameters in LAI estimation.

Despite there are limitations, such as regional dependency, of the VI approach in vegetation variables remote sensing retrieval,

the increasing availability of broad and narrow spectral bands from satellite sensors is driving the continuing development of VI because of its simplicity and robustness [37]. Considering that an increasing number of satellite sensors (e.g., the upcoming Landsat-10) may include red-edge bands [62], multispectral red-edge VI is promising for improving the LAI estimation accuracy and efficiency at the regional scale. Since the spatial resolution of existing LAI products and datasets is mostly kilometer to hectometer [47], [63], [64], the proposed multispectral red-edge VIs provide promising solutions to fast achieve decameter LAI results within the region of interest and at the time of interest by using the Sentinel-2 images, especially with the aid of the cloud-computing platform such as the Google Earth Engine [65], [66]. This enhancement of spatial resolution will be highly beneficial for some certain applications, for example, the precision agriculture, which need more LAI spatial details.

VI. Conclusion

The red-edge bands in the multispectral satellite sensors hold great potential for improving the accuracy of LAI retrievals. In this study, chlorophyll insensitive multispectral red-edge VIs for Sentinel-2/MSI and GF-6/WFV were developed to capture LAI variations from the perspectives of reducing the LCC impacts and saturation effects. The optimal bands in proposed SR-like, NDVI-like, and MSR-like red-edge VIs for LAI estimation were selected first by using the correlation analysis and EFAST sensitivity analysis approaches based on the PROSAIL model. Then, the responses of proposed multispectral red-edge VIs to the LAI and LCC were simulated by PROSAIL and analyzed comprehensively. Finally, the performance of those VIs in deriving LAI was further evaluated using ground measured LAI, and they were compared with those obtained with other widely used VIs. The results suggest that they exhibited a high sensitivity to LAI variations and low sensitivity to LCC variations, thus are suitable for empirically-based crop LAI retrieval. However, further effects are still need in a more comprehensive evaluation and validation with more ground data in various biome types. This study demonstrated the importance of considering red-edge bands in VI-based LAI retrievals, and the results are promising for providing a decameter LAI dataset for more accurate fine-scale ecosystem modeling and agricultural applications.

Acknowledgment

The authors would like to thank the Sentinel Scientific Data Hub for providing Sentinel-2/MSI data and the software and algorithm for atmospheric correction, and the China Centre for Resources Satellite Data and Application for providing GF-6/WFV data, and Earth Science Data Systems (ESDS) Program of NASA for providing MODIS LAI data.

References

[1] S. Piao et al., "Characteristics, drivers and feedbacks of global greening," *Nature Rev. Earth Environ.*, vol. 1, no. 1, pp. 14–27, 2020, doi: 10.1038/s43017-019-0001-x.

[2] J. Xiao et al., "Remote sensing of the terrestrial carbon cycle: A review of advances over 50 years," *Remote Sens. Environ.*, vol. 233, Nov. 2019, Art. no. 111383, doi: 10.1016/j.rse.2019.111383.

[3] J. M. Chen and T. A. Black, "Defining leaf area index for non-flat leaves," *Plant Cell Environ.*, vol. 15, no. 4, pp. 421–429, 1992, doi: 10.1111/j.1365-3040.1992.tb00992.x.

[4] H. Fang, F. Baret, S. Plummer, and G. Schaepman-Strub, "An overview of global leaf area index (LAI): Methods, products, validation, and applications," *Rev. Geophys.*, vol. 57, no. 3, pp. 739–799, Sep. 2019, doi: 10.1029/2018rg000608.

[5] R. B. Myneni et al., "Global products of vegetation leaf area and fraction absorbed PAR from year one of MODIS data," *Remote Sens. Environ.*, vol. 83, no. 1, pp. 214–231, 2002, doi: 10.1016/S0034-4257(02)00074-3.

[6] Z. Zhu et al., "Greening of the Earth and its drivers," *Nature Climate Change*, vol. 6, no. 8, pp. 791–795, 2016, doi: 10.1038/nclimate3004.

[7] C. Chen et al., "China and India lead in greening of the world through land-use management," *Nature Sustainability*, vol. 2, no. 2, pp. 122–129, 2019, doi: 10.1038/s41893-019-0220-7.

[8] G. Yan et al., "Review of indirect optical measurements of leaf area index: Recent advances, challenges, and perspectives," *Agricultural Forest Meteorol.*, vol. 265, pp. 390–411, 2019, doi: 10.1016/j.agrformet.2018.11.033.

[9] Z. Xiao et al., "Use of general regression neural networks for generating the GLASS leaf area index product from time-series MODIS surface reflectance," *IEEE Trans. Geosci. Remote Sens.*, vol. 52, no. 1, pp. 209–223, Jan. 2014, doi: 10.1109/TGRS.2013.2237780.

[10] Y. Sun, Q. Qin, H. Ren, T. Zhang, and S. Chen, "Red-edge band vegetation indices for leaf area index estimation from Sentinel-2/MSI imagery," *IEEE Trans. Geosci. Remote Sens.*, vol. 58, no. 2, pp. 826–840, Feb. 2020, doi: 10.1109/TGRS.2019.2940826.

[11] J. Verrelst et al., "Optical remote sensing and the retrieval of terrestrial vegetation bio-geophysical properties—A review," *ISPRS J. Photogrammetry Remote Sens.*, vol. 108, pp. 273–290, 2015, doi: 10.1016/j.isprsjprs.2015.05.005.

[12] R. Houborg, M. McCabe, A. Cescatti, F. Gao, M. Schull, and A. Gitelson, "Joint leaf chlorophyll content and leaf area index retrieval from Landsat data using a regularized model inversion system (REGFLEC)," *Remote Sens. Environ.*, vol. 159, pp. 203–221, 2015, doi: 10.1016/j.rse.2014.12.008.

[13] K. Berger et al., "Evaluation of the PROSAIL model capabilities for future hyperspectral model environments: A review study," *Remote Sens.*, vol. 10, no. 1, 2018, Art. no. 85. [Online]. Available: https://www.mdpi.com/2072-4292/10/1/85

[14] S. Jacquemoud et al., "PROSPECT+SAIL models: A review of use for vegetation characterization," *Remote Sens. Environ.*, vol. 113, pp. S56–S66, 2009, doi: 10.1016/j.rse.2008.01.026.

[15] Y. Sun, H. Ren, T. Zhang, C. Zhang, and Q. Qin, "Crop leaf area index retrieval based on inverted difference vegetation index and NDVI," *IEEE Geosci. Remote Sens. Lett.*, vol. 15, no. 11, pp. 1662–1666, Nov. 2018, doi: 10.1109/LGRS.2018.2856765.

[16] F. Wang et al., "Estimation of above-ground biomass of winter wheat based on consumer-grade multi-spectral UAV," *Remote Sens.*, vol. 14, no. 5, 2022, Art. no. 1251. [Online]. Available: https://www.mdpi.com/2072-4292/14/5/1251

[17] D. N. H. Horler, M. Dockray, and J. Barber, "The red edge of plant leaf reflectance," *Int. J. Remote Sens.*, vol. 4, no. 2, pp. 273–288, 1983, doi: 10.1080/01431168308948546.

[18] C. Wu, Z. Niu, Q. Tang, and W. Huang, "Estimating chlorophyll content from hyperspectral vegetation indices: Modeling and validation," *Agricultural Forest Meteorol.*, vol. 148, no. 8, pp. 1230–1241, 2008, doi: 10.1016/j.agrformet.2008.03.005.

[19] D. Heckmann, U. Schlüter, and A. P. M. Weber, "Machine learning techniques for predicting crop photosynthetic capacity from leaf reflectance spectra," *Mol. Plant*, vol. 10, no. 6, pp. 878–890, 2017, doi: 10.1016/j.molp.2017.04.009.

[20] O. Sytar et al., "Applying hyperspectral imaging to explore natural plant diversity towards improving salt stress tolerance," *Sci. Total Environ.*, vol. 578, pp. 90–99, 2017, doi: 10.1016/j.scitotenv.2016.08.014.

[21] J. Delegido, J. Verrelst, C. M. Meza, J. P. Rivera, L. Alonso, and J. Moreno, "A red-edge spectral index for remote sensing estimation of green LAI over agroecosystems," *Eur. J. Agronomy*, vol. 46, pp. 42–52, 2013, doi: 10.1016/j.eja.2012.12.001.

[22] Q. Xie et al., "Leaf area index estimation using vegetation indices derived from airborne hyperspectral images in winter wheat," *IEEE J. Sel. Topics Appl. Earth Observ. Remote Sens.*, vol. 7, no. 8, pp. 3586–3594, Aug. 2014, doi: 10.1109/JSTARS.2014.2342291.

[23] L. Liang et al., "Estimation of crop LAI using hyperspectral vegetation indices and a hybrid inversion method," *Remote Sens. Environ.*, vol. 165, pp. 123–134, 2015, doi: 10.1016/j.rse.2015.04.032.

[24] H. Yuan et al., "Retrieving soybean leaf area index from unmanned aerial vehicle hyperspectral remote sensing: Analysis of RF, ANN, and SVM regression models," *Remote Sens.*, vol. 9, no. 4, 2017, Art. no. 309. [Online]. Available: https://www.mdpi.com/2072-4292/9/4/309

[25] Z. Chen et al., "Leaf area index estimation algorithm for GF-5 hyperspectral data based on different feature selection and machine learning methods," *Remote Sens.*, vol. 12, no. 13, 2020, Art. no. 2110. [Online]. Available: https://www.mdpi.com/2072-4292/12/13/2110

[26] L. Liang et al., "Estimating crop LAI using spectral feature extraction and the hybrid inversion method," *Remote Sens.*, vol. 12, no. 21, 2020, Art. no. 3534. [Online]. Available: https://www.mdpi.com/2072-4292/12/21/3534

[27] B. Lu, P. D. Dao, J. Liu, Y. He, and J. Shang, "Recent advances of hyperspectral imaging technology and applications in agriculture," *Remote Sens.*, vol. 12, no. 16, 2020, Art. no. 2659. [Online]. Available: https://www.mdpi.com/2072-4292/12/16/2659

[28] Y. Gu et al., "Multimodal hyperspectral remote sensing: An overview and perspective," *Sci. China Inf. Sci.*, vol. 64, no. 2, 2021, Art. no. 121301, doi: 10.1007/s11432-020-3084-1.

[29] A. Kross, H. McNairn, D. Lapen, M. Sunohara, and C. Champagne, "Assessment of RapidEye vegetation indices for estimation of leaf area index and biomass in corn and soybean crops," *Int. J. Appl. Earth Observ. Geoinformation*, vol. 34, pp. 235–248, 2015, doi: 10.1016/j.jag.2014.08.002.

[30] T. Dong et al., "Assessment of red-edge vegetation indices for crop leaf area index estimation," *Remote Sens. Environ.*, vol. 222, pp. 133–143, 2019, doi: 10.1016/j.rse.2018.12.032.

[31] F. Li et al., "Improving estimation of summer maize nitrogen status with red edge-based spectral vegetation indices," *Field Crops Res.*, vol. 157, pp. 111–123, 2014, doi: 10.1016/j.fcr.2013.12.018.

[32] Y. Zhu et al., "Exploring the potential of WorldView-2 red-edge band-based vegetation indices for estimation of Mangrove leaf area index with machine learning algorithms," *Remote Sens.*, vol. 9, no. 10, 2017, Art. no. 1060. [Online]. Available: https://www.mdpi.com/2072-4292/9/10/1060

[33] M. Drusch et al., "Sentinel-2: ESA's optical high-resolution mission for GMES operational services," *Remote Sens. Environ.*, vol. 120, pp. 25–36, 2012, doi: 10.1016/j.rse.2011.11.026.

[34] W. J. Frampton, J. Dash, G. Watmough, and E. J. Milton, "Evaluating the capabilities of Sentinel-2 for quantitative estimation of biophysical variables in vegetation," *ISPRS J. Photogrammetry Remote Sens.*, vol. 82, pp. 83–92, 2013, doi: 10.1016/j.isprsjprs.2013.04.007.

[35] X. Jiang, S. Fang, X. Huang, Y. Liu, and L. Guo, "Rice mapping and growth monitoring based on time series GF-6 images and red-edge bands," *Remote Sens.*, vol. 13, no. 4, 2021, Art. no. 579. [Online]. Available: https://www.mdpi.com/2072-4292/13/4/579

[36] W. Yu, P. Zhao, K. Xu, Y. Zhao, P. Shen, and J. Ma, "Evaluation of red-edge features for identifying subtropical tree species based on Sentinel-2 and Gaofen-6 time series," *Int. J. Remote Sens.*, vol. 43, no. 8, pp. 3003–3027, 2022, doi: 10.1080/01431161.2022.2079018.

[37] Y. Zeng et al., "Optical vegetation indices for monitoring terrestrial ecosystems globally," *Nature Rev. Earth Environ.*, vol. 3, no. 7, pp. 477–493, 2022, doi: 10.1038/s43017-022-00298-5.

[38] I. Herrmann, A. Pimstein, A. Karnieli, Y. Cohen, V. Alchanatis, and D. J. Bonfil, "LAI assessment of wheat and potato crops by VENμS and Sentinel-2 bands," *Remote Sens. Environ.*, vol. 115, no. 8, pp. 2141–2151, 2011, doi: 10.1016/j.rse.2011.04.018.

[39] S. T. Brantley, J. C. Zinnert, and D. R. Young, "Application of hyperspectral vegetation indices to detect variations in high leaf area index temperate shrub thicket canopies," *Remote Sens. Environ.*, vol. 115, no. 2, pp. 514–523, 2011, doi: 10.1016/j.rse.2010.09.020.

[40] N. Xing et al., "A transformed triangular vegetation index for estimating winter wheat leaf area index," *Remote Sens.*, vol. 12, no. 1, 2020, Art. no. 16. [Online]. Available: https://www.mdpi.com/2072-4292/12/1/16

[41] Q. Xie et al., "Vegetation indices combining the red and red-edge spectral information for leaf area index retrieval," *IEEE J. Sel. Topics Appl. Earth Observ. Remote Sens.*, vol. 11, no. 5, pp. 1482–1493, May 2018, doi: 10.1109/JSTARS.2018.2813281.

[42] J. B. Féret, A. A. Gitelson, S. D. Noble, and S. Jacquemoud, "PROSPECT-D: Towards modeling leaf optical properties through a complete lifecycle," *Remote Sens. Environ.*, vol. 193, pp. 204–215, 2017, doi: 10.1016/j.rse.2017.03.004.

[43] W. Verhoef, L. Jia, Q. Xiao, and Z. Su, "Unified optical-thermal four-stream radiative transfer theory for homogeneous vegetation canopies," *IEEE Trans. Geosci. Remote Sens.*, vol. 45, no. 6, pp. 1808–1822, Jun. 2007, doi: 10.1109/TGRS.2007.895844.

[44] J. Markwell, J. C. Osterman, and J. L. Mitchell, "Calibration of the Minolta SPAD-502 leaf chlorophyll meter," *Photosynthesis Res.*, vol. 46, no. 3, pp. 467–472, 1995, doi: 10.1007/BF00032301.

[45] R. Houborg and E. Boegh, "Mapping leaf chlorophyll and leaf area index using inverse and forward canopy reflectance modeling and SPOT reflectance data," *Remote Sens. Environ.*, vol. 112, no. 1, pp. 186–202, 2008, doi: 10.1016/j.rse.2007.04.012.

[46] K. Yan et al., "Evaluation of MODIS LAI/FPAR product collection 6. Part 1: Consistency and improvements," *Remote Sens.*, vol. 8, no. 5, 2016, Art. no. 359. [Online]. Available: https://www.mdpi.com/2072-4292/8/5/359

[47] Y. Knyazikhin, J. V. Martonchik, R. B. Myneni, D. J. Diner, and S. W. Running, "Synergistic algorithm for estimating vegetation canopy leaf area index and fraction of absorbed photosynthetically active radiation from MODIS and MISR data," *J. Geophysical Res.: Atmos.*, vol. 103, no. D24, pp. 32257–32275, 1998, doi: 10.1029/98jd02462.

[48] H. Varella, M. Guérif, and S. Buis, "Global sensitivity analysis measures the quality of parameter estimation: The case of soil parameters and a crop model," *Environ. Model. Softw.*, vol. 25, no. 3, pp. 310–319, 2010, doi: 10.1016/j.envsoft.2009.09.012.

[49] A. Saltelli, S. Tarantola, and K. P. S. Chan, "A quantitative model-independent method for global sensitivity analysis of model output," *Technometrics*, vol. 41, no. 1, pp. 39–56, 1999, doi: 10.1080/00401706.1999.10485594.

[50] C. F. Jordan, "Derivation of leaf-area index from quality of light on the forest floor," *Ecology*, vol. 50, no. 4, pp. 663–666, 1969, doi: 10.2307/1936256.

[51] J. W. Rouse, R. H. Haas, J. A. Schell, and D. W. Deering, "Monitoring vegetation systems in the great plains with ERTS," in *Proc. 3rd Earth Resour. Technol. Satell.-1 Symp.- Volume I: Tech. Presentations*, 1974, pp. 3010–3017.

[52] J. M. Chen, "Evaluation of vegetation indices and a modified simple ratio for boreal applications," *Can. J. Remote Sens.*, vol. 22, no. 3, pp. 229–242, 1996, doi: 10.1080/07038992.1996.10855178.

[53] Y. Zeng et al., "Spectral invariant provides a practical modeling approach for future biophysical variable estimations," *Remote Sens.*, vol. 10, no. 10, Oct. 2018, Art. no. 1508, doi: 10.3390/rs10101508.

[54] G. Badgley, C. B. Field, and J. A. Berry, "Canopy near-infrared reflectance and terrestrial photosynthesis," *Sci. Adv.*, vol. 3, no. 3, 2017, Art. no. e1602244, doi: 10.1126/sciadv.1602244.

[55] J. Sui et al., "Winter wheat production estimation based on environmental stress factors from satellite observations," *Remote Sens.*, vol. 10, no. 6, 2018, Art. no. 962, doi: 10.3390/rs10060962.

[56] Y. Sun et al., "Seasonal and long-term variations in leaf area of Congolese rainforest," *Remote Sens. Environ.*, vol. 268, 2022, Art. no. 112762, doi: 10.1016/j.rse.2021.112762.

[57] Q. Xie et al., "Retrieval of crop biophysical parameters from Sentinel-2 remote sensing imagery," *Int. J. Appl. Earth Observation Geoinformation*, vol. 80, pp. 187–195, 2019, doi: 10.1016/j.jag.2019.04.019.

[58] T. Majasalmi and M. Rautiainen, "The potential of Sentinel-2 data for estimating biophysical variables in a boreal forest: A simulation study," *Remote Sens. Lett.*, vol. 7, no. 5, pp. 427–436, 2016, doi: 10.1080/2150704X.2016.1149251.

[59] J. G. P. W. Clevers, L. Kooistra, and M. M. M. Van den Brande, "Using Sentinel-2 data for retrieving LAI and leaf and canopy chlorophyll content of a potato crop," *Remote Sens.*, vol. 9, no. 5, 2017, Art. no. 405. [Online]. Available: https://www.mdpi.com/2072-4292/9/5/405

[60] J. G. P. W. Clevers, L. Kooistra, and M. M. M. van den Brande, "Using Sentinel-2 data for retrieving LAI and leaf and canopy chlorophyll content of a potato crop," *Remote Sens.*, vol. 9, no. 5, May 2017, Art. no. 405, doi: 10.3390/rs9050405.

[61] J. Delegido, J. Verrelst, L. Alonso, and J. Moreno, "Evaluation of Sentinel-2 red-edge bands for empirical estimation of green LAI and chlorophyll content," *Sensors*, vol. 11, no. 7, pp. 7063–7081, 2011. [Online]. Available: https://www.mdpi.com/1424-8220/11/7/7063

[62] Z. Wu et al., "User needs for future Landsat missions," *Remote Sens. Environ.*, vol. 231, 2019, Art. no. 111214, doi: 10.1016/j.rse.2019.111214.

[63] F. Baret et al., "GEOV1: LAI and FAPAR essential climate variables and FCOVER global time series capitalizing over existing products. Part1: Principles of development and production," *Remote Sens. Environ.*, vol. 137, pp. 299–309, 2013, doi: 10.1016/j.rse.2012.12.027.

[64] K. Yan et al., "Generating global products of LAI and FPAR from SNPP-VIIRS data: Theoretical background and implementation," *IEEE Trans. Geosci. Remote Sens.*, vol. 56, no. 4, pp. 2119–2137, Apr. 2018, doi: 10.1109/tgrs.2017.2775247.

[65] N. Gorelick, M. Hancher, M. Dixon, S. Ilyushchenko, D. Thau, and R. Moore, "Google Earth Engine: Planetary-scale geospatial analysis for everyone," *Remote Sens. Environ.*, vol. 202, pp. 18–27, 2017, doi: 10.1016/j.rse.2017.06.031.

[66] Y. Sun, Q. Qin, H. Ren, and Y. Zhang, "Decameter cropland LAI/FPAR estimation from Sentinel-2 imagery using Google Earth Engine," *IEEE Trans. Geosci. Remote Sens.*, vol. 60, 2022, Art. no. 4400614, doi: 10.1109/TGRS.2021.3052254.

Yuanheng Sun received the Ph.D. degree in cartography and GIS from Peking University, Beijing, China, in 2021.

He is currently an Assistant Professor with the Environmental Information Institute, Navigation College, Dalian Maritime University, Dalian, China. His research interests focus on remote sensing of vegetation and coastal wetland.

Binyu Wang received the B.E. degree in computer science and technology from Jilin University, Changchun, China, in 2021. He is currently working toward the M.E. degree with the School of Navigation, Dalian Maritime University, Dalian, China.

His research interests include coastal wetland remote sensing.

Zhaoxu Zhang was born in Hebei, China. He received the M.S. degree in surveying engineering from China University of Geosciences (Beijing), Beijing, China, in 2016 and the Ph.D. degree in GIS from Peking University, Beijing, China, in 2021.

He is currently a Lecturer of the School of Environmental Science and Engineering, Tiangong University, Tianjin, China. His main research interests include agricultural drought monitoring and soil moisture retrieval.